RSC Advances

PAPER

View Article Online
View Journal | View Issue

Cite this: *RSC Adv.*, 2026, **16**, 16389

Low-energy densification of carbon anodes for fluorine electrolysis applications *via* a multi-cycle impregnation–carbonization route

Zhenfei Ma,[a] Xiankui Yang,[e] Jiangtao Zhu,[e] Xingjian Kong*[bc] and Pan Zhang *[d]

Hard-to-control energy input and reliability trade-offs in conventional multi-high-temperature routes hinder densification of carbon anodes used in high-temperature electrochemical systems such as fluorine electrolysis, and the coupling between process parameters, pore evolution and properties remains insufficiently resolved. Here we report a scalable tri-impregnation semi-carbonization plus one final carbonization route that lowers peak carbonization stresses while maintaining densification efficiency. An infiltration framework that treats open/closed pores as vertical/horizontal capillaries and explicitly accounts for quinoline-insoluble (QI) filter-cake formation is established based on Darcy's law to quantify permeability evolution. A viscosity–temperature/thermogravimetric dual window delineates the wetting/filling regime while suppressing premature pyrolysis; in parallel, a bubble-escape-limited porogenesis mechanism rationalizes the role of heating ramps and isothermal holds on pore-size distribution and density gradients. Guided by these analyses, optimized parameters (impregnation at 210 °C, 1 MPa, 30 min; delayed heating in 300–500 °C) increase volume density, build a percolated conductive network, and mitigate swelling/cracking. The bulk resistivity decreases from 52.7 to 32.1 μΩ m, while compressive strength improves; density uniformity shows ΔD_{max} = 0.010–0.020 g cm^{-3} in early cycles, increasing to 0.042 g cm^{-3} later, indicating the need for staged pressure/temperature holds to enhance deep-zone densification. The resulting process-structure–property map defines transferable parameter windows and quality-control metrics, offering a low-energy, industry-ready route to high-reliability carbon anodes suitable for fluorine electrolysis and related high-temperature electrochemical processes.

Received 17th September 2025
Accepted 11th November 2025

DOI: 10.1039/d5ra07043k

rsc.li/rsc-advances

1. Introduction

Under the "dual-carbon" (carbon peaking and carbon neutrality) goals and the ongoing upgrading of the fluorochemicals sector, industrial fluorine electrolysis imposes more stringent requirements on the electrical, mechanical, and service stability of its key component—the carbon anode.[1–3] The anode's bulk density, pore architecture, and microstructural ordering not only govern current distribution and fluorine bubble detachment, but also directly affect anodic polarization, the frequency of anode effects, the specific energy consumption of fluorine production, and overall process safety.[4–6] In current engineering practice, multi-step high-temperature carbonization routes such as the "two-impregnation/three-carbonization" process can increase anode densification to some extent, but they entail high fuel consumption and thermal shock to equipment; moreover, periodic installation and replacement of anodes in the cell keep the life-cycle cost high.[7,8] How to markedly reduce preparation energy consumption while simultaneously improving densification efficiency, density uniformity, and service reliability remains a key scientific and engineering challenge for the fluorine industry.

Prior studies have largely focused on materials and surfaces—for example, improving the petroleum coke/pitch matrix, applying coatings or micro-textures to suppress fluorination and facilitate bubble detachment, and optimizing the coupled electric- and flow-fields at the cell scale to mitigate anode effects.[9–11] However, a full-process perspective that systematically elucidates how impregnation-carbonization parameters couple to densification efficiency and properties across"preparation process, pore evolution, microstructure, electro/mechanical performance, service behavior" is still lacking.[12,13] In particular, the governing role of quinoline-insoluble (QI)-dominated filter-cake effects on re-opening of pores and infiltration resistance in high-density preforms remains

[a]*Purification Equipment Research Institute of CSSC, Handan, China*
[b]*Chemical Science and Engineering College, Sichuan University, Chengdu 610065, China. E-mail: kongxingjian@scu.edu.cn*
[c]*Engineering Research Center of Comprehensive Utilization and Clean Processing of Phosphorus, Chengdu 610065, P. R. China*
[d]*College of Chemical Engineering, Sichuan University of Science & Engineering, Zigong 643000, China. E-mail: 18381314085@163.com*
[e]*Peric Special Gases Co., Ltd, Handan, Hebei 056002, China*

unclear;[14,15] the coupling boundaries defined by the pitch viscosity–temperature spectrum and thermogravimetric (TG) windows for wetting/filling *versus* pyrolysis-induced porosity require quantitative delimitation;[16,17] and validated parameter windows and quality-control criteria are still needed to map how carbonization heating schedules and staged isothermal holds regulate pore-size distribution,[18,19] connectivity, and the surface–interior density gradient (ΔD_{max}), as well as how microcrystalline parameters (d_{002}, L_a, L_c) correlate with resistivity and compressive strength.[20]

Building on these insights, this work targets mid-temperature fluorine production lines and proposes a low-energy densification route aimed at reducing peak carbonization temperature and fuel consumption, while systematically investigating how processing influences densification efficiency and performance of carbon anodes. The core concept is a "three impregnation-semi-carbonization cycles plus one impregnation–final carbonization" scheme: within appropriate pressure and temperature windows, staged mitigation of pyrolysis, optimization of heating rates, and isothermal holds are employed to achieve continuous pore filling, manage thermal stresses, and coordinate microstructural ordering. Accordingly, a multiscale correlation framework—linking process parameters → pore structure → microstructural ordering → macroscopic properties—is established. Combined with modeling and experimental characterization, scale-up-oriented parameter windows and key quality-control points are provided.

The main research contents and innovations are summarized as follows:

(1) Low-peak-temperature densification route: a "three semi-carbonizations plus one final carbonization" process is proposed and validated, lowering peak carbonization temperature and total carbonization time while maintaining electro/mechanical performance, thereby balancing energy use, thermal shock to equipment, and continuous production needs.

(2) Preform infiltration and flow model: open/closed pores are abstracted as vertical/horizontal capillaries; a QI filter-cake formation mechanism is introduced; and an effective permeability description and criterion for high-density preforms are developed on the basis of Darcy's law. Proxy tests using G5-grade filter crucibles are employed to estimate the effective permeability of pitch.

(3) Dual window for "wettability–anti-pyrolysis": by combining the pitch viscosity–temperature curve with TG analysis, three regimes—melting/softening, steady-state flow, and pyrolytic decomposition—are delineated, defining temperature windows and holding strategies that favor wetting/filling while suppressing gas-forming decomposition, thus guiding thermal control of the process.

(4) Porogenesis mechanism and density-gradient control: a bubble-escape-limited porogenesis mechanism is validated *via* fracture-surface morphology and thermal analysis. The effects of heating schedules and staged isothermal holds on pore-size distribution, connectivity, and ΔD_{max} are clarified, and a process path is proposed to enhance density uniformity.

(5) Process–structure–property mapping: the influences of carbonization time/heating schedule, maximum carbonization temperature, impregnation time/temperature/pressure, and preform mass (size) on bulk density, resistivity, compressive strength, and density uniformity are systematically evaluated. Parameter combinations and quality indices suitable for engineering scale-up are established to realize the co-optimization of densification efficiency and service performance.

2. Experimental section

2.1. Materials

The petroleum coke used in this study was supplied by Tianjin Youhao New Materials Technology Co., Ltd (China), and its trace element composition is listed in Table 1. The pitch was a modified pitch provided by Shanghai Baosteel Chemical Co., Ltd (China), with its specific properties summarized in Table 2.

2.2. Sample preparation

The pulverized petroleum coke was graded according to the particle-size distribution in Table 3 and blended accordingly. The coke and pitch were then charged into a kneader-mixer and mixed at 180 °C for 30 min to ensure that the pitch fully coated and wetted the coke particle surfaces. The mixed batch was hot-pressed to form cylindrical green compacts with uniform diameter and height. Specifically, the green bodies obtained by hot pressing were first calcined under a nitrogen atmosphere at a heating rate of 2 k min^{-1} up to 300 °C to obtain semi-carbonized samples. These samples were then immersed in molten pitch preheated to 220 °C, with nitrogen pressure applied up to 1 MPa for 55 min of impregnation. After impregnation, the samples were again calcined under nitrogen at 300 °C with a heating rate of 2 k min^{-1}. This impregnation-calcination process was repeated three times under identical conditions. Finally, the samples were carbonized under nitrogen at 800 °C with a heating rate of 10 k min^{-1} to obtain the final products.

Table 1 Composition of trace elements in petroleum coke

Elements	Fe	S	K	Ca	Ni
Wt.(%)	0.224	1.79	0.0225	0.273	0.208

Table 2 Properties of modified asphalt

Properties	Index
β-resin insolubles (%)	0.27
Softening point (°C)	109.4
Moisture (%)	4.07
Ash content (%)	0.27
Quinoline insolubles (%)	8.6
Carbon residue (%)	39.51
Coking yield (%)	57.20

Table 3 Particle size distribution of petroleum coke

Particle size range (mm)	Ball-milled powder	0.054–0.075	0.075–0.15	0.15–0.355	0.355–0.6	0.6–0.7
Ratio	5	4	1	1	2	2

2.3. Testing details

Microstructures were observed by scanning electron microscopy (SEM, TESCAN VEGA3 SBH). Phase compositions were characterized by X-ray diffraction (XRD, Empyrean, PANalytical). Thermal decomposition was examined using a simultaneous thermal analyzer (Netzsch STA 449 F3) under nitrogen (N_2). The electrical resistivity of carbon plates was measured with a four-point probe (KDB-1). The open porosity of the carbon anodes was determined according to the standard boiling water method (YS/T 63.6). Compressive properties before and after use were tested on a universal testing machine (Instron 5967). Pitch viscosities at different temperatures were measured with a digital viscometer (DV-2). Unless otherwise specified, all measurements were performed at room temperature.

3. Results

3.1. Coupled mechanism of mass transfer during preform impregnation and porogenesis during carbonization

To address the poor pitch mass transfer encountered in the impregnation stage of low-density carbon anodes, we first establish an equivalent capillary-channel model governed by open/closed pores (Fig. 1). Low-density preforms are dominated by large-aperture open pores, whereas high-density preforms comprise ~90% open pores with a small fraction of closed pores; the diameter of open pores spans 0.01–100 μm. During impregnation, open pores are treated as vertical capillary bundles connected to the external surface, while closed pores are regarded as horizontal capillary bundles without external connectivity.[21,22] The following assumptions are adopted: (i) the preform geometry remains unchanged under external pressure; (ii) the liquid pitch is incompressible; (iii) the fluid within the pore channels is continuous and saturated at all times; and (iv) the effective capillary channels are approximately straight. This model reveals a primary "particle-pore size" matching constraint for impregnation effectiveness: when the size of quinoline-insoluble (QI) particles is smaller than the diameter of open pores, they can be carried inward with the fluid; otherwise, they accumulate at pore mouths to form a filter cake, markedly increasing infiltration resistance—thereby explaining the root cause of incomplete filling in high-density preforms.

Considering the difficulty of directly measuring the permeability of the QI filter cake, a G5 filter crucible with a comparable pore-size scale was employed as an equivalent surrogate. Based on Darcy's law and mass conservation, a measurable expression for the permeability was established, with the derivation given in eqn (1)–(5). Experimental results (Fig. S1) show that, in the early stage of impregnation, small QI particles are carried out with the fluid and deposit at pore mouths to form an initial filter cake with high porosity and thus high permeability; in the mid-stage, continued accumulation of fine particles on the cake sharply constricts the flow channels, leading to a rapid decrease in permeability; in the late stage, the cake becomes substantially densified, only a few open pores sustain flow, and the permeability approaches a very low level. This "fast-to-slow" permeability kinetics is consistent with the microscopic process of stepwise sieving/accumulation of QI particles.[23]

The slow infiltration of liquid in micropores is described by Darcy's law:[24]

$$K = \frac{\varepsilon \mu v d}{\Delta p} \tag{1}$$

where d and Δp denote the filter-cake thickness and the pressure drop between its upper and lower surfaces, respectively.

From mass conservation, it follows that:

$$d = \frac{w_p \rho_L x}{\rho_p (1-\varepsilon) - w_p \rho_L} \tag{2}$$

where w_p is the mass fraction of quinoline insolubles (QI), and x is the drop in the pitch liquid level within the crucible.

From the definition of flow velocity, we have:

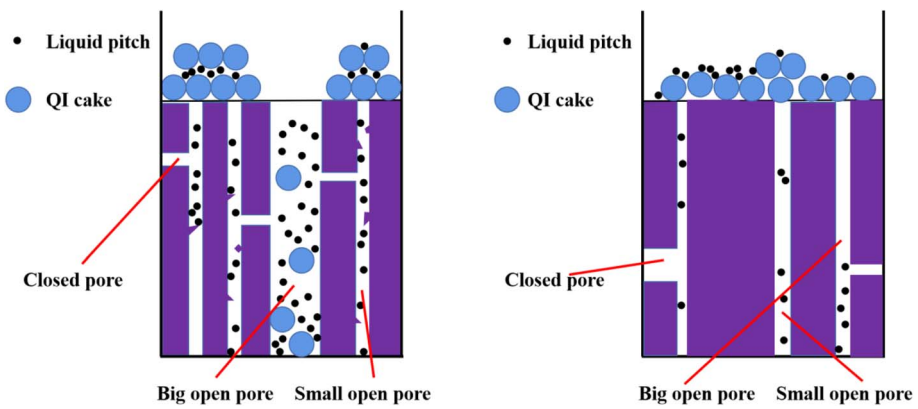

Fig. 1 Impregnation model of preform (low density preform on left and high density preform on right).

$$v = \frac{dx}{dt} \quad (3)$$

$$B = \frac{w_p \rho_L}{\rho_p(1-\varepsilon) - w_p \rho_L} \quad (4)$$

By combining eqn (1)–(4) and integrating, the following expression is obtained:

$$K = \frac{\varepsilon \mu B x^2}{2\Delta p t} \quad (5)$$

The rheological properties of pitch play a decisive role in impregnation behavior. As shown in Fig. S2, its viscosity–temperature curve exhibits a distinct three-stage feature: 130–190 °C corresponds to the melting–softening region, where viscosity drops sharply beyond the softening point, favoring wetting and spreading; 190–230 °C is the steady-flow region, where physicochemical properties remain stable and wetting/filling efficiency is maximized; at ≥230 °C, the system enters the pyrolysis/aging region, where the evolution of pyrolysis gases not only reduces the internal negative pressure and effective pressure drop within the preform, but may also trigger bubble phase transitions, thereby weakening impregnation efficiency. This indicates that the impregnation temperature window should not be raised indiscriminately but rather balanced between achieving low viscosity and suppressing pyrolysis. The pore formation during carbonization can be explained by the bubble-escape-limited mechanism (Fig. S3).[17,25] Pyrolysis of pitch continuously generates bubbles: those near the surface escape under internal pressure, while those within the bulk remain constrained by the solid skeleton, grow progressively, and eventually leave residual pores upon solidification or rupture. A comparison of gas evolution with TG mass loss (Fig. 2) shows that the onset temperature of gas release lags behind that of the corresponding weight loss, reflecting a temporal mismatch between "generation–migration–escape" and "weight loss–solidification". Based on TG characteristics, the carbonization process can be divided into three stages:

Stage I (≤230 °C): softening and stress relaxation with minor volatilization;

Stage II (230–400 °C): intense pyrolysis and gas release, followed by polycondensation into semicoke at 400–500 °C during this stage the heating rate should be reduced to avoid cracking;

Stage III (500–700 °C, extending to 700–1200 °C): transformation from semicoke to coke and progressive graphitization.

This staged understanding provides both thermodynamic and kinetic guidance for setting subsequent process parameters.

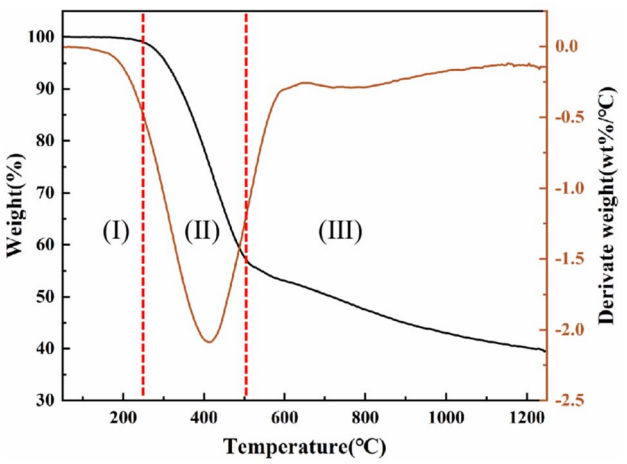

Fig. 2 TG curve of asphalt pyrolysis.

3.2. Influence and optimization of impregnation–carbonization parameters on the densification of carbon anodes

With carbonization pressure, impregnation time, and impregnation temperature kept under controlled boundary conditions, the effects of heating schedule, maximum carbonization temperature, impregnation time/temperature, applied pressure, and preform size on densification efficiency and dimensional stability were systematically investigated. Based on these analyses, a low-energy, reproducible optimization route was constructed.

First, regarding the heating schedule (Table S1 and Fig. 3), introducing a delay (*i.e.*, a slower heating ramp) in the 300–500 °C interval significantly enhanced bulk density while suppressing volumetric expansion. This is because this temperature range corresponds to the main reaction stage of polycondensation and semicoke formation; a slower heating rate not only facilitates the orderly release of pyrolysis gases, thereby reducing macroscopic tensile stresses induced by internal pressure, but also promotes the growth and alignment of mesophase domains, thus improving the continuity of conductive and thermal pathways. By contrast, the 0–300 °C range (dominated by softening/flow) and the 500 °C isothermal stage (subsequent semicoke-to-coke conversion) exhibited weaker effects on density and expansion. Therefore, considering overall performance and cost, the B3 heating profile was identified as the optimal scheme.

Second, the maximum carbonization temperature directly determines both the pore "re-opening" capacity and the interfacial bonding quality for the subsequent impregnation cycle (Fig. 4). Experimental results show that a single impregnation–1200 °C carbonization step yields a bulk density increment of 0.131 g cm^{-3}, which is comparable to the cumulative increment obtained from three successive impregnation–500 °C semi-carbonization cycles. Considering energy consumption, production rhythm, and equipment limitations, a cyclic route of three impregnation–500 °C semi-carbonizations followed by one final carbonization is proposed. This strategy significantly reduces peak temperature and specific energy consumption without sacrificing densification effectiveness.

Next, a pronounced coupling effect was observed between impregnation time and preform size (Fig. 5a–f). As the preform

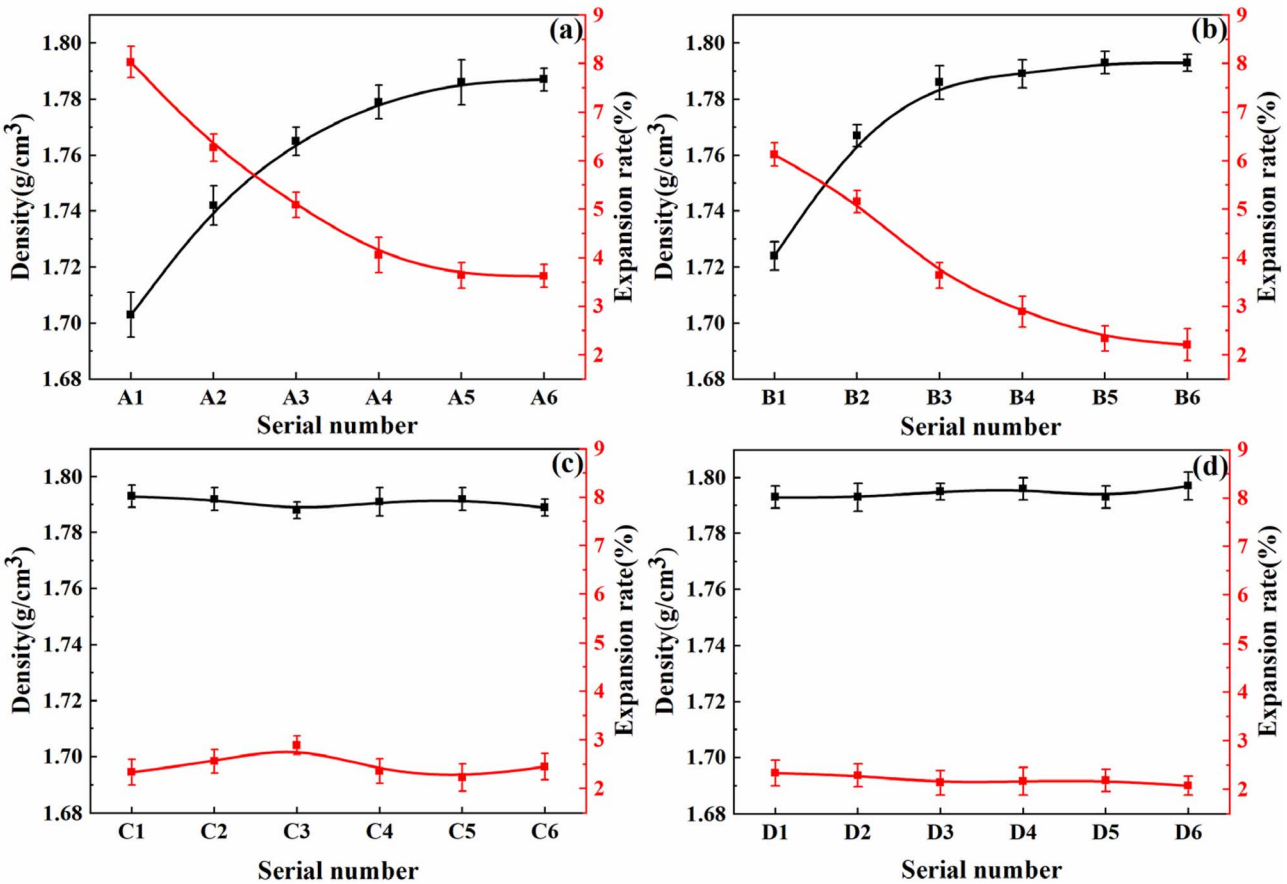

Fig. 3 Influence of carbonization time on volume expansion rate and volume density (a) is the temperature range from 400 to 500 °C; (b) is the temperature range from 300 to 400 °C; (c) is the temperature range from 0 to 300 °C; (d) is constant temperature at 500 °C.

size increased, the internal network complexity, wall friction, and pressure drop also increased, resulting in decreased impregnation efficiency. For smaller samples, the density gain gradually leveled off after a certain time, showing a "time marginal effect". Balancing infiltration depth, structural uniformity, and production rhythm, a forming mass of 5 g and an impregnation time of 30 min were selected as the baseline conditions for subsequent experiments and scale-up validation.

In addition, impregnation temperature and applied pressure represent two key "direct control variables" governing wetting and penetration. The results (Fig. 5g, S4a and b) show that with increasing impregnation temperature, the impregnation rate and bulk density first increased and then decreased, compressive strength first increased and then decreased, while resistivity first decreased and then increased. The inflection point corresponded to the transition between the rheological steady state and the onset of pyrolysis. Balancing low viscosity, effective wetting/spreading, and resistance to pyrolysis, 210 °C was identified as the optimal impregnation temperature.

Regarding pressure (Fig. 5h), in low-density preforms dominated by large pores with lower capillary resistance, the benefit of applying additional pressure was limited. In contrast, in high-density preforms dominated by micropores/cracks, external pressure significantly enhanced infiltration depth and densification efficiency. Considering efficiency and cost, 1 MPa was selected as the standard impregnation pressure.

Finally, a global comparison of the new and conventional routes (Table S2) showed that the new process, employing four cycles instead of the conventional two, significantly reduces peak carbonization temperature to 500 °C, shortens effective carbonization duration, and improves impregnation sufficiency, while simultaneously lowering energy consumption. Thus, the new route offers superior techno-economic performance and better compatibility with industrial equipment.

3.3. Testing data and performance characterization of carbon anodes

As shown in Fig. S4, the bulk resistivity of carbon anodes decreases continuously with the cyclic impregnation–carbonization process. During the first three "impregnation–semi-carbonization" cycles, the rate of decrease gradually slows; after the fourth "impregnation-final carbonization," the resistivity drops from 52.7 μΩ m to 32.1 μΩ m, a reduction of 39.1%, indicating a significant improvement in electrical conductivity. Mechanistically, this can be explained by the tunneling conduction effect and percolation-network theory:[26,27] initially, particle spacing is relatively large and pore connectivity is poor, leading to high macroscopic resistivity. As pitch gradually fills the pores and carbonizes,

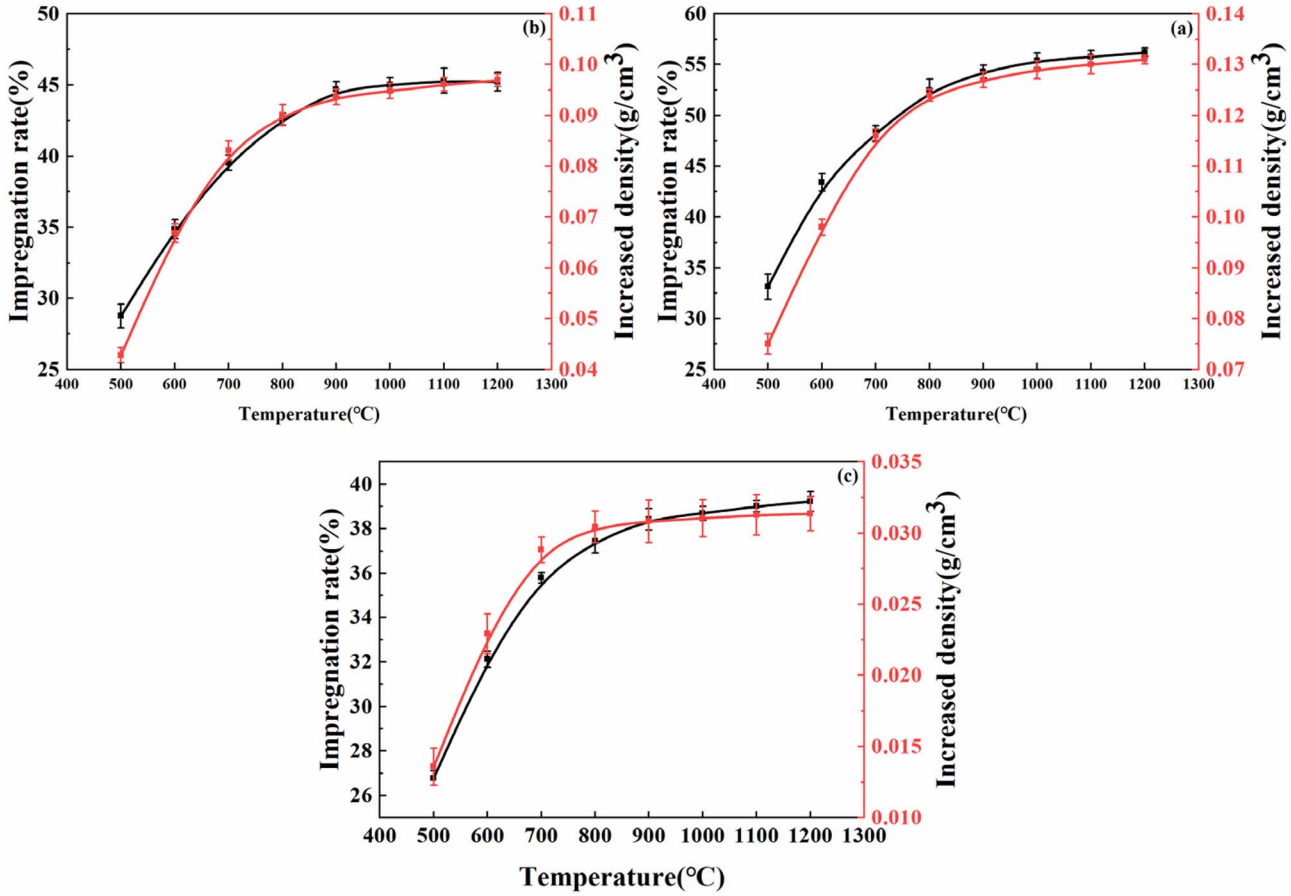

Fig. 4 Influence of carbonization temperature on impregnation effect and volume density (a) is the first impregnation-carbonization stage, (b) is the second impregnation-carbonization stage, (c) is the third impregnation-carbonization stage.

the effective interparticle spacing decreases; when the gap narrows to only tens of nanometers, electrons can quantum-tunnel through thin layers to form local conductive pathways. Once connectivity surpasses the percolation threshold, a three-dimensional conductive network rapidly develops, resulting in a sharp drop in resistivity. Thereafter, additional pitch primarily modifies the network and passivates defects, leading to a slower rate of decrease. Upon completion of carbonization, the transformation from semicoke to coke further stabilizes and broadens the conduction paths, driving resistivity lower.

Fig. 6a shows the compressive strength at different impregnation–carbonization cycles. Overall, compressive strength increases with the number of cycles: pores are progressively filled, pore number and size are reduced, the load-bearing capacity of the skeleton is enhanced, and stress concentration is alleviated. The "pseudo-plastic fracture" observed after the first impregnation–semi-carbonization gradually transitions into "brittle fracture" as densification advances, reflecting the enhanced interfacial bonding and improved wall continuity that reshape load-bearing and energy-release mechanisms. In low-density samples, early failure is mainly initiated at large pores and weak interfaces; after densification, this effect is significantly mitigated, resulting in improved macroscopic strength stability.

The XRD patterns of samples at different cycles are shown in Fig. 6b, and the corresponding lattice parameters are listed in Table S3. With increasing cycle number, the (002) peak shifts to smaller angles, d_{002} gradually increases, while L_a and L_c decrease, indicating microcrystalline refinement and adjustment of structural ordering. This result is consistent with the combined effects of "pore filling–carbonization densification–microcrystalline rearrangement". Correlations among L_a, L_c, porosity (ε), compressive strength, and electrical resistivity were subsequently fitted. The fitting results reveal that porosity exhibits a stronger correlation with both compressive strength and resistivity. This is because, with increasing impregnation cycles, the pitch undergoes carbonization to form a three-dimensional network structure. The interwoven network strengthens the inter-particle connections, thereby enhancing the mechanical properties and reducing electrical resistance (Fig. S5).

It should be noted that excessively high carbonization temperatures may induce microcrystalline structures that can form covalent bonds with fluorine atoms during electrolysis, disrupting the extended π-bond network of carbon layers. This would sharply reduce electronic conductivity and eventually lead to the formation of an insulating layer on the carbon anode surface, which is detrimental to stable fluorine production.

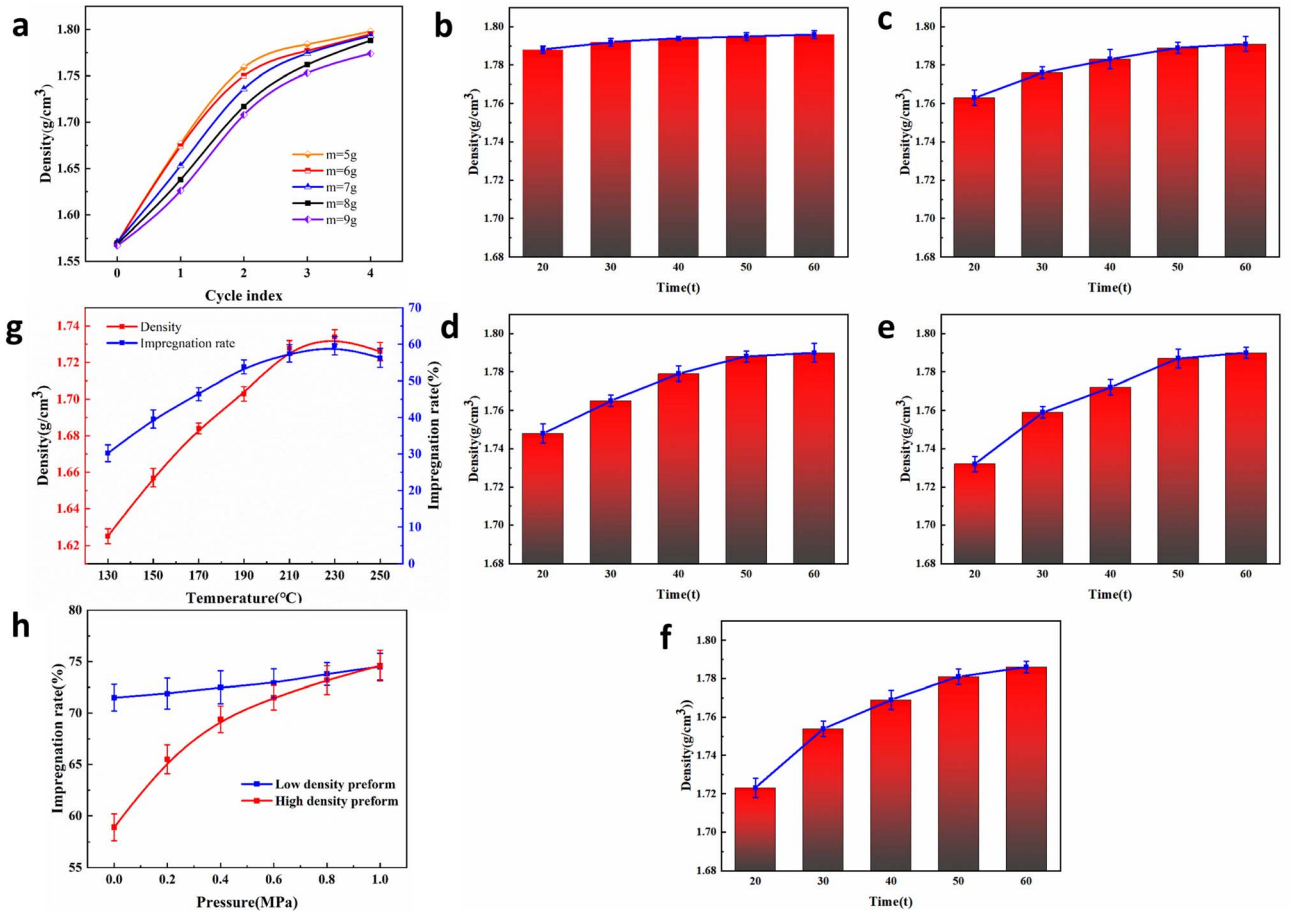

Fig. 5 (a)Influence of forming quality (preform size) on cyclic impregnation-carbonization; (b–f)Influence of impregnation time on volume density ((b) is 5 g; (c) is 6 g; (d) is 7 g; (e) is 8 g; (f) is 9 g; (g) influence of impregnation pressure on impregnation rate; (h) influence of impregnation pressure on impregnation rate.

Therefore, the carbonization temperature of carbon anodes for fluorine electrolysis should be strictly controlled below 1600 °C.[21,28]

Density uniformity was evaluated using the symmetric thickness-reduction method to prepare test blocks of different heights, and densities were calculated by the volume–weight method.[29,30] The parameters of the green bodies at different impregnation–carbonization cycles are listed in Table S4, and the corresponding test results are summarized in Tables S5–S8. The results show that after the first two "impregnation–semi-carbonization" cycles, the maximum density difference (ΔD_{max})

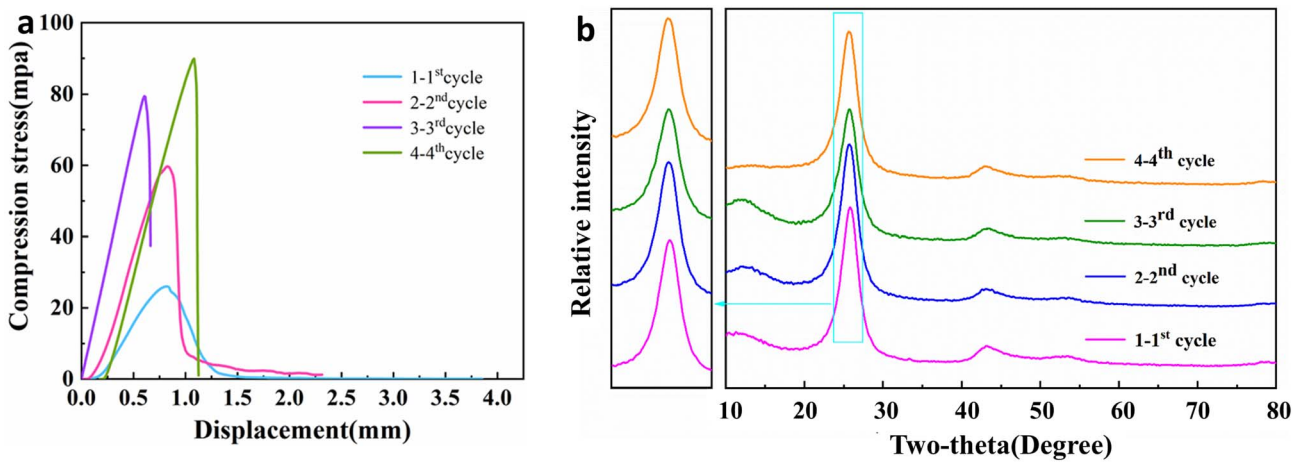

Fig. 6 (a) Compressive strength of preforms at different cycles of impregnation and carbonation; (b) XRD patterns of preforms under different cycles of impregnation and carbonization.

was 0.010–0.020 g cm^{-3}, indicating good uniformity. After the third and fourth cycles, ΔD_{max} increased to 0.028 g cm^{-3} and 0.042 g cm^{-3}, respectively, and exhibited a density-decreasing gradient from the surface toward the interior as the sample thickness was reduced (Fig. 7). This phenomenon indicates that in the later stages, surface regions densify preferentially, while deep penetration is hindered by both infiltration resistance and filter-cake densification, resulting in a gradient-type density distribution. Such carbon anode density inhomogeneity may lead to localized high current density, thereby affecting the overall performance and lifetime of the anode, especially in large-scale, high-load industrial electrolyzers. To mitigate this gradient in future scale-up scenarios, strategies such as designing electrode structures with graded porosity or directional channels could be employed to guide a more uniform distribution of ion flow. Overall, density uniformity is strongly correlated with impregnation penetration depth; in the later cycles, strategies such as staged pressurization or tailored temperature–holding profiles may also be employed to further enhance deep-zone densification.

For ease of discussion, Fig. S6 illustrates the fracture morphology evolution of carbon anodes at different impregnation–carbonization stages. As shown in Fig. S5 ((1–1)–(1–3)), after the first "impregnation–semi-carbonization", the fracture surface exhibits a pronounced coral-like structure, with numerous large pores and voids, as well as interspersed small pores forming partially interconnected channels. Such defects mainly arise from the combined effects of pyrolysis gas release and thermal stresses during carbonization: the former accumulates and escapes within the skeleton, while the latter induces microcrack propagation under temperature gradients and phase-change shrinkage. Together, these processes lead to the formation and amplification of the pore structure. At the macroscopic level, these pores disrupt the continuity of effective conductive pathways, resulting in increased bulk resistivity and higher energy consumption during operation. When anode effects occur during electrolysis, it is often necessary to briefly increase the voltage (approximately 3–5 min) to strip off the surface fluorinated passivation layer. Under the combined influence of electrolyte flushing and thermal flow, the aforementioned pores and microcracks serve as preferential initiation sites for crack propagation, significantly compromising service reliability. From a processing perspective, multiple impregnation–carbonization cycles are therefore required to reduce the defect volume fraction and enhance structural densification, thereby improving corrosion resistance and anti-polarization capability.

A further comparison of Fig. S5 ((1–1), (2–1), (3–1), and (4–1)) shows that with increasing impregnation–carbonization cycles, the fracture morphology gradually transitions from rough and porous to flat and dense: large pores are markedly reduced, small pores are progressively filled, and ultimately only a few fine micropores remain. Compared with commonly used resin-based impregnating agents, pitch exhibits superior wetting and spreading behavior on pore walls and aggregates during impregnation. After high-temperature carbonization, the resulting pitch-derived carbon forms strong adhesion and mechanical interlocking with the pore walls, enhancing particle–matrix interfacial bonding strength, tightening particle connections, and thereby constructing continuous load-bearing and conductive networks. The evolution of fracture morphology and the reduction in pore size/number are consistent with the observed improvements in macroscopic electrical and mechanical properties, providing direct microstructural evidence. To verify the high reliability of the carbon anode material during fluorine electrolysis, we conducted practical operation tests of the prepared carbon anode in an industrial electrolyzer and systematically evaluated the changes in its compressive strength before and after operation. The test results show that the compressive strength of the carbon anode decreased from the initial 93 MPa to 71 MPa after operation. Despite this reduction, the post-operation sample still maintained good mechanical performance, indicating that the material possesses high structural stability under the harsh conditions of fluorine electrolysis.

Table S9 compares the properties of samples prepared by the new and conventional processes with those of typical fluorine-electrolysis carbon anodes from multiple countries. The new-process samples meet the basic requirements for Chinese fluorine-electrolysis anodes in terms of bulk density, resistivity, compressive strength, ash content, and porosity, while occupying a relatively favorable range compared to international samples. Given the significant advantages of the new route in lowering peak carbonization temperature and reducing energy consumption, this process can satisfy the requirements of mid-temperature fluorine-electrolysis production lines and offers a feasible pathway for cost-effective industrial production.

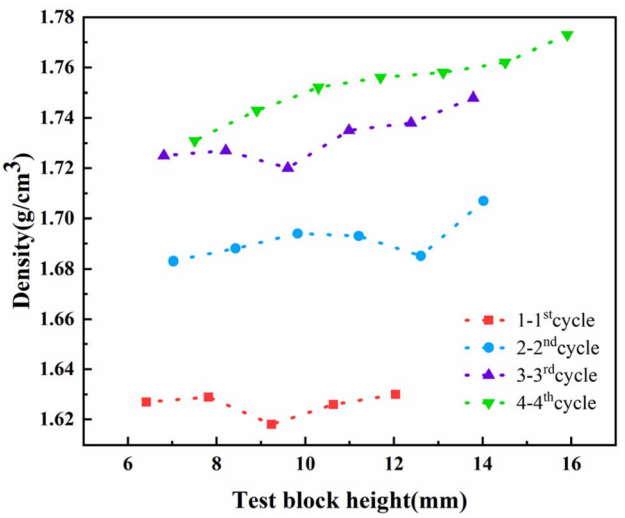

Fig. 7 Test block density distribution.

4. Conclusion

This study proposes and validates a low-energy densification route for carbon anodes in industrial fluorine electrolysis, namely a "three impregnation–semi-carbonizations plus one final carbonization" process. By combining a capillary

infiltration model, a dual viscosity–temperature/TG window, fracture morphology, and XRD analyses, the coupling mechanisms between processing parameters, pore evolution, microstructural ordering, and macroscopic properties were systematically revealed. Scalable parameter ranges and quality-control criteria were also established. The main conclusions are as follows:

Low-energy densification process: compared with conventional multi-step high-temperature carbonization, the proposed route reduces peak carbonization temperature and energy consumption while maintaining densification efficiency and mechanical performance, with advantages in continuous production and equipment compatibility.

Mass transfer and QI effect: an equivalent infiltration model based on Darcy's law was developed, revealing the "fast-to-slow" permeability kinetics caused by QI filter-cake formation.

Dual window and heating optimization: three regimes—melting–softening, steady-state flow, and pyrolysis decomposition—were clarified. An impregnation temperature of 210 °C was identified as optimal; a slower heating ramp in the 300–500 °C range facilitated gas release and densification, with the B3 profile showing superior performance.

Performance enhancement and structure correlation: under optimized conditions, bulk resistivity decreased from 52.7 to 32.1 μΩ m and compressive strength improved. XRD revealed microcrystalline refinement and reordering. Density uniformity was good in early cycles but showed a surface-to-core gradient in later cycles, suggesting staged pressurization or tailored temperature–holding strategies to further improve deep-zone densification.

In summary, a multiscale framework linking process parameters–pore structure–properties has been constructed. The proposed low-energy and scalable fabrication route provides both theoretical guidance and practical pathways for performance enhancement and green manufacturing of carbon anodes for fluorine electrolysis.

Conflicts of interest

The authors declare that they have no known competing financial interests or personal relationships that could have appeared to influence the work reported in this paper.

Data availability

No data was used for the research described in the article.

Supplementary information (SI) is available. See DOI: https://doi.org/10.1039/d5ra07043k.

Acknowledgements

The authors gratefully acknowledge Dr Yongming Shen for his valuable assistance in proofreading and language polishing of the manuscript.

References

1 M. Ikram, M. Ferasso, R. Sroufe and Q. Zhang, Assessing green technology indicators for cleaner production and sustainable investments in a developing country context, *J. Cleaner Prod.*, 2021, **322**, 129090, DOI: 10.1016/j.jclepro.2021.129090.

2 J. Inamoto, S. Enoki, A. Inoo, N. Tamura and Y. Matsuo, Promise of dual carbon batteries with graphene-like graphite as both electrodes, *Carbon*, 2024, **216**, 118512, DOI: 10.1016/j.carbon.2023.118512.

3 A. Hussein, D. Picard and H. Alamdari, Biopitch as a Binder for Carbon Anodes: Impact on Carbon Anode Properties, *ACS Sustainable Chem. Eng.*, 2021, **9**, 4681–4687, DOI: 10.1021/acssuschemeng.1c00618.

4 A. Kamiyama, K. Kubota, D. Igarashi, Y. Youn, Y. Tateyama, H. Ando, K. Gotoh and S. Komaba, MgO-template synthesis of extremely high capacity hard carbon for na-ion battery, *Angew. Chem-Ger. Edit.*, 2021, **133**, 5174–5180, DOI: 10.1002/ange.202013951.

5 Y. Wu, H. Liu, D. Li, R. Dong, M. Bu, B. Liu, X. Fan and W. Zhang, LiF-rich solid electrolyte interface induced by fluorinated carbon enables stable silicon anodes with high initial coulombic efficiency, *Chem. Eng. J.*, 2025, **522**, 167558, DOI: 10.1016/j.cej.2025.167558.

6 P. Zhang, J. Wang, Y. Shu, W. Fu, Y. Wang, J. Ye and L. Yang, Design of a high-efficiency electrolytic energy conversion system based on equilibrium analysis of electric-field and flow-field through simulation and experiments, *Energy Convers. Manage.*, 2023, **277**, 116679, DOI: 10.1016/j.enconman.2023.116679.

7 J. Drofenik, M. Gaberščček, R. Dominko, M. Bele and S. Pejovnik, Carbon anodes prepared from graphite particles pretreated in a gelatine solution, *J. Power Sources*, 2001, **94**, 97–101, DOI: 10.1016/S0378-7753(00)00651-0.

8 J. Xiao, J. Li, S. Ye, Y. Lai and Y. Liu, Laboratory study of property-modified prebaked carbon anode and application in large aluminum electrolysis cells, *J. Cent. South Univ.*, 2005, **12**, 68–71, DOI: 10.1007/s11771-005-0374-5.

9 H. Quan, S. Sui, L. Wang, R. Luo and X. Dong, A low-temperature preparation strategy of SiC/ZrB2-CrSi2-Si/SiC multilayer oxidation-resistant coating for C/C composites: Process, kinetics and mechanism research, *Appl. Surf. Sci.*, 2021, **562**, 149993, DOI: 10.1016/j.apsusc.2021.149993.

10 J. Yang, J. Li, T. Wang, P. H. L. Notten, H. Ma, Z. Liu, C. Wang and G. Wang, Novel hybrid of amorphous Sb/N-doped layered carbon for high-performance sodium-ion batteries, *Chem. Eng. J.*, 2021, **407**, 127169, DOI: 10.1016/j.cej.2020.127169.

11 H. Tebibel, Methodology for multi-objective optimization of wind turbine/battery/electrolyzer system for decentralized clean hydrogen production using an adapted power management strategy for low wind speed conditions, *Energy Convers. Manage.*, 2021, **238**, 114125, DOI: 10.1016/j.enconman.2021.114125.

12 T. Falcon, N. Batisse, M. Dubois, K. Guérin, A. Jourdan and H. Groult, Micro-texturing by femtosecond laser ablation of a carbonaceous anode for production of fluorine by electrolysis, *J. Fluorine Chem.*, 2021, **244**, 109746, DOI: 10.1016/j.jfluchem.2021.109746.

13 C. Hu, P. Zhang, X. Wang, X. Yang, L. Yang, Z. Zhang and X. Kong, Improvement of fluidization quality of a LiF bed using internal blades, *Powder Technol.*, 2020, **362**, 817–825, DOI: 10.1016/j.powtec.2019.12.008.

14 Y. Lu, D. Kocaefe, Y. Kocaefe, X.-A. Huang and D. Bhattacharyay, The wettability of coke by pitches with different quinoline-insoluble contents, *Fuel*, 2017, **199**, 587–597, DOI: 10.1016/j.fuel.2017.03.019.

15 R. Moriyama, J.-i. Hayashi and T. Chiba, Effects of quinoline-insoluble particles on the elemental processes of mesophase sphere formation, *Carbon*, 2004, **42**, 2443–2449, DOI: 10.1016/j.carbon.2004.04.044.

16 G. Li, J. Yang, B. Zhang, Y. Li, Y. Zhao, H. Zhang and Y. Wang, Effect of hydrogenation on coal tar pitch structures and mesophase rheological properties for improving spinning performance, *Carbon*, 2025, **238**, 120219, DOI: 10.1016/j.carbon.2025.120219.

17 J. Yang, P. A. Tanguy and C. Roy, Heat transfer, mass transfer and kinetics study of the vacuum pyrolysis of a large used tire particle, *Chem. Eng. Sci.*, 1995, **50**, 1909–1922, DOI: 10.1016/0009-2509(95)00062-A.

18 S. Gustafsson and A. Mihranyan, Strategies for tailoring the pore-size distribution of virus retention filter papers, *ACS Appl. Mater. Interfaces*, 2016, **8**, 13759–13767, DOI: 10.1021/acsami.6b03093.

19 Z. Gou, Y. Zuo, M. Tian and W. Lin, Siloxane-Based Nanoporous Polymers with Narrow Pore-size Distribution for Cell Imaging and Explosive Detection, *ACS Appl. Mater. Interfaces*, 2018, **10**, 28979–28991, DOI: 10.1021/acsami.8b08582.

20 M. Brandl, M. H. Sayed, C. Chory, I. Hammer-Riedel, J. Parisi, R. Hock and L. Gütay, In-situ XRD investigation of selenization of CZTS nanoparticles, *J. Alloys Compd.*, 2017, **714**, 35–38, DOI: 10.1016/j.jallcom.2017.04.199.

21 M. Zhang, H. Liu, T. Ma, Z. Song and S. Shao, Ultrathin porous Mn(PO3)2 nanosheets and MoO2 nanocrystal arrays on N, P-dual-doped graphene for high-energy asymmetric supercapacitors, *Chem. Eng. J.*, 2021, **403**, 126379, DOI: 10.1016/j.cej.2020.126379.

22 J. Peng, H. Wang, X. Shi and H. J. Fan, Ultrahigh Plateau-Capacity Sodium Storage by Plugging Open Pores, *Adv. Mater.*, 2024, 2410326, DOI: 10.1002/adma.202410326.

23 J. Gonçalvès, S. Violette, C. Robin, D. Bruel, F. Guillocheau and E. Ledoux, Combining a compaction model with a facies model to reproduce permeability fields at the regional scale, *Phys. Chem. Earth Parts A/B/C 29*, 2004, 17–24, DOI: 10.1016/j.pce.2003.11.009.

24 Y. Endo, D.-R. Chen and D. Y. H. Pui, Theoretical consideration of permeation resistance of fluid through a particle packed layer, *Powder Technol.*, 2002, **124**, 119–126, DOI: 10.1016/S0032-5910(01)00479-X.

25 K. Zhang, P. Lu, X. Guo, L. Wang, H. Lv, Z. Wang and Y. He, High-temperature pyrolysis behavior of two different rank coals in fixed-bed and drop tube furnace reactors, *J. Energy Inst.*, 2020, **93**, 2271–2279, DOI: 10.1016/j.joei.2020.06.010.

26 M. Jiang, B. Zhou and X. Wang, Comparisons and validations of contact angle models, *Int. J. Hydrogen Energy*, 2018, **43**, 6364–6378, DOI: 10.1016/j.ijhydene.2018.02.016.

27 H.-J. Butt, J. Liu and K. Koynov, Contact angle hysteresis, *Interface Sci.*, 2022, **59**, 101574.

28 A. Tressaud, F. Moguet, S. Flandrois, M. Chambon, C. Guimon, G. Nanse, E. Papirer, V. Gupta and O. P. Bahl, On the nature of C□F bonds in various fluorinated carbon materials: XPS and TEM investigations, *J. Phys. Chem. Solids*, 1996, **57**, 745–751, DOI: 10.1016/0022-3697(96)00343-5.

29 H. Tebibel, Methodology for multi-objective optimization of wind turbine/battery/electrolyzer system for decentralized clean hydrogen production using an adapted power management strategy for low wind speed conditions, *Energy Convers. Manage.*, 2021, **238**, 114125, DOI: 10.1016/j.enconman.2021.114125.

30 J. Yang, J. Li, T. Wang, P. H. L. Notten, H. Ma, Z. Liu, C. Wang and G. Wang, Novel hybrid of amorphous Sb/N-doped layered carbon for high-performance sodium-ion batteries, *Chem. Eng. J.*, 2021, **407**, 127169, DOI: 10.1016/j.cej.2020.127169.